Structure of Macroscopic Monodomains and Its Soft Confinements of Chiral Smectic Phases on Crystallization in a Main-Chain Nonracemic Liquid Crystalline Polyester

Shi Jin,[†] Kwang-Un Jeong,[‡] Yingfeng Tu, Matthew J. Graham, Jing Wang, Frank W. Harris, and Stephen Z. D. Cheng*

Maurice Morton Institute and Department of Polymer Science, The University of Akron, Akron, Ohio 44325-3909

Received April 6, 2007; Revised Manuscript Received May 22, 2007

ABSTRACT: A main-chain nonracemic chiral liquid crystalline (LC) polyester was synthesized using an A−B type condensation reaction of a chiral monomer, *R*-(−)4′-{ω-[2-(*p*-hydroxy-*o*-nitrophenyloxy)-1-propyloxy]-1-heptyloxy}-4-biphenylcarboxylic acid, and was abbreviated as PET(R*-7). Wide-angle X-ray diffraction (WAXD) experiments combined with differential scanning calorimetry measurements revealed multiple phase transitions including a chiral twist grain boundary A (TGBA*) phase, a chiral smectic A (SmA*) phase, a chiral smectic C (SmC*) phase, and a highly ordered monoclinic crystalline (K_M) phase with decreasing temperature. Flat-elongated and right-handed double-twisted helical single crystals were grown thermotropically in the smectic LC states. Both crystal types possessed the identical monoclinic unit cell: $a = 1.04$ nm, $b = 0.46$ nm, $c = 5.59$ nm, $\alpha = \beta = 90°$, and $\gamma = 84.2°$ based on the WAXD and selected area electron diffraction results. Uniaxial elongation of centimeter-sized films (along the *xz*-plane in a three-dimensional, 3D, coordinate system) of submillimeter thickness (along the *y*-axis) resulted in macroscopic smectic monodomains. Analysis of the detailed 2D WAXD results indicated that in the SmA* phase the molecules are parallel to the layer normal in the direction of elongation. However, in the SmC* phase, the 3D macroscopic monodomain was constructed with the layers which possess a 13° synclinically tilted layer normal with respect to the elongation direction (the *z*-axis). The molecules in the 3D monodomains of SmC* phase were tilted ∼8° synclinically with respect to the elongation direction within the "in-plane" of the film (within the *xz*-plane), translating to a ∼21° tilt with respect to the layer normal. During the crystallization of the K_M phase in the SmA* phase, the *c*-axis of the K_M crystal is along the elongation direction (the *z*-axis), yet the *d*-spacing of the (00*l*) (*l* = even number) planes were slightly larger than the layer spacing of the SmA* phase. When the crystallization occurred in the 3D monodomain of the SmC* phase, on the other hand, the synclinically tilted LC layers and the tilted layer normal orientation with respect to the elongation direction (the *z*-axis) were retained in the K_M crystal, although the *d*-spacing of the (00*l*) (*l* = even number) planes was larger than the layer spacing of the SmC* phase. The most striking observation was that in order to form the K_M crystals in the SmC* phase the molecules must undergo a remarkable reorientation (∼21° tilting) to became a single-crystal-like monodomain while retaining the synclinically tilted layer structure.

Introduction

Natural materials, such as polypeptides, proteins, deoxyribonucleic acid, and ribonucleic acid, have been instructional for chemists and physicists in designing and synthesizing programmed molecular structures and their organization into superstructures.[1−10] One of the most important aspects of natural and synthetic materials is chiral interactions and chirality transfer from the subnanometer to micrometer length scales.[11−20] Similar to the hierarchy of natural materials, four length scales of chiralty for synthesized materials have been established. Even though many scientists have devoted their effort to understanding the different levels of chirality and the transfer of chirality between length scales, we do not yet have a complete understanding of these processes.

Recently, our group has demonstrated these four levels of chirality in a series of specifically designed main-chain nonracemic chiral liquid crystalline (LC) polyesters synthesized from (*R*)-(−)-4′-{ω-[2-(*p*-hydroxy-*o*-nitrophenyloxy)-1-propyloxy]-1-nonyloxy}-4-biphenylcarboxylic acid [abbreviated as PET(R*-*n* or S*-*n*), where *n* is the number of methylene units].[21−30] In this system, we found that the handedness of the helical sense is determined not only by the configurational chirality but also by the number of methylene units. For example, both PET(S*-9) and PET(R*-10) exhibited left-handed helical crystals, while PET(R*-9) formed right-handed helical crystals. Utilizing dark-field transmission electron microscopy (TEM) and selected area electron diffraction (SAED) techniques, we identified that the chain orientation in these helical crystals was twisted along both the long and short axes (double twist), and the chirality transfer between the different length scales has been determined to be dependent upon the packing scheme within each of the length scales.

In this publication, we extend our study of the series to *R*-(−)-4′-{ω-[2-(*p*-hydroxy-*o*-nitrophenyloxy)-1-propyloxy]-1-heptyloxy}-4-biphenylcarboxylic acid, PET(R*-7), a main-chain nonracemic chiral polyester with a right-handed configurational chirality and an odd number of methylene carbons ($n = 7$). On the basis of wide-angle X-ray diffraction (WAXD) and SAED experiments combined with differential scanning calorimetry (DSC), it was determined that this polyester possesses a monoclinic crystalline phase (K_M) with flat-elongated and right-

* To whom the correspondence should be addressed. E-mail: scheng@uakron.edu.

[†] Current address: Department of Chemistry, College of Staten Island, The City University of New York, Staten Island, NY 10314,

[‡] Current address: Advanced Molecular Engineering for Optoelectronics, Department of Polymer Nano Science and Technology, Chonbuk National University, Jeonju, 561-756, Korea.

10.1021/ma070821p CCC: $37.00
Published on Web 06/21/2007

hand twisted helical single crystals,[21−29] along with three low-ordered LC phases including a chiral twist grain boundary A (TGBA*) phase, a chiral smectic A (SmA*) phase, and a chiral smectic C (SmC*) phase, similar to our previous results.[22,24,28,29]

Since the helical single crystals can be formed in either the SmA* or SmC* phase, we are interested in investigating how the K_M crystals form within the precursor smectic LC phases. In particular, we are going to focus on the relationships between the chain orientations in the crystalline K_M phase and in the layer structures of these smectic LC phases. In order to carry out this study, we prepared the samples with smectic LC monodomains on the scale of centimeters for our two-dimensional (2D) WAXD experiments and grew single crystals for our SAED experiments. Experimental results indicate that the layer structures and molecular orientations in both of the precursor smectic phases significantly affect the *c*-axis orientation of the K_M crystals. This reveals that the crystal formation is confined in these two smectic LC phases.

Experimental Section

Materials and Sample Preparation. A nonracemic chiral main-chain LC PET(R*-7) polyester was synthesized from *R*-(−)-4′-{*ω*-[2-(*p*-hydroxy-*o*-nitrophenyloxy)-1-propyloxy]-1-heptyloxy}-4-biphenylcarboxylic acid via an A−B type condensation polymerization. This polyester consisted of a flexible spacer with seven methylene units ($n = 7$) and a mesogen with biphenyl and phenyl groups linked by an ester group. The chiral carbon (configurational chirality) in PET(R*-7) had the R-absolute (right-handed) spatial configuration, and this isoregio arrangement of the chiral centers is ensured by the A−B type condensation polymerization. The detailed synthetic procedures can be found in ref 31. The chemical structure of PET(R*-7) polyester is the following:

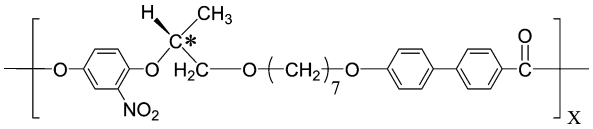

The number-average molecular weight of PET(R*-7) was ∼20 kg/mol, and the polydispersity was ∼2 after fractionation, as measured by gel permeation chromatography based on polystyrene standards. The samples were kept in vacuum before carrying out characterization and analysis. For DSC experiments, the sample weight was about 2 mg, and the pan weights were kept constant at a precision of ±0.001 mg. In order to observe the evolution of different phase structures, a structurally isotropic film of PET(R*-7) with a thickness of 0.5 mm was prepared in the melt for one-dimensional (1D) WAXD powder experiments. Monodomain film samples were uniaxially elongated 300% in the SmA* and SmC* phases and annealed in these phases at constant lengths for prolonged times. 2D WAXD experiments were performed to determine the phase structures and to investigate the confinement effect during the crystallization process. The typical dimensions of the monodomain film for 2D WAXD experiments were 0.2 mm × 1 mm × 3 mm. Thin film samples were prepared for TEM by solution-casting PET(R*-7)/tetrahydrofuran solution (0.05 g/L) onto a carbon-coated mica surface. The film thickness ranged between 50 and 100 nm. The samples were then heated to their isotropic melt and then quenched to predetermined crystallization temperatures for isothermal crystallization. After crystallization, the films were floated on the water surface and recovered using copper TEM grids. Some of the samples were further shadowed with Pt for TEM morphological observations.

Equipment and Experiments. The thermal transitions were studied using a Perkin-Elmer PYRIS Diamond DSC with an Intracooler 2P apparatus. The temperatures and heat flows were calibrated using material standards (benzoic acid and indium) at cooling and heating rates ranging from 2.5 to 20 °C/min. The heating experiments always preceded the cooling experiments in order to eliminate previous thermal histories, and the cooling and heating rates were kept identical. The transition temperatures were determined by measuring the onset and peak temperatures from both the cooling and heating scans at different rates.

1D WAXD experiments were conducted in the reflection mode of a Rigaku 12 kW rotating-anode X-ray (Cu Kα radiation) generator coupled to a diffractometer. The diffraction peak positions and widths were calibrated with silicon crystals of known crystal size in the high 2θ angle region (>15°) and silver behenate in the low 2θ angle region. A hot stage was coupled to the diffractometer in order to study the structural evolutions during cooling and heating. The temperature of this hot stage was calibrated to be within ±1 °C. Samples were scanned across a 2θ angle ranging from 1.5° to 40° at a scanning rate of 4°/min.

In order to determine the phase structures and orientations, 2D WAXD experiments on the mechanically microextruded and uniaxially drawn film samples were conducted using an imaging system (Rigaku, R-AXIS-IV) with an 18 kW rotating anode X-ray generator. A hot stage was also used to obtain diffraction patterns in the LC phase at elevated temperatures. A 30 min exposure time was required for a high-quality pattern. In both 1D and 2D WAXD experiments, background scattering was subtracted from the sample scans.

Bright-field TEM images (JEOL, 1200 EX II) were obtained to examine crystal morphology on the nanometer scale using an accelerating voltage of 120 kV. SAED patterns of the single-crystal samples were obtained to determine the crystal unit-cell symmetry and dimensions. The camera length was set at 50 cm, with the SAED calibrated for *d*-spacings smaller than 0.384 nm using evaporated thallous chloride. Spacing values larger than 0.384 nm were calibrated by doubling the *d*-spacing values of the first-order diffractions of thallous chloride.

The Cerius[2] (version 4.6) simulation software from Accelrys was used to calculate the energy-minimized geometry of PET(R*-7) in the isolated gas phase utilizing the COMPASS force field. Overlapped thermal transition peaks in DSC and merged scattering halos in 2D WAXD were resolved using the PeakFit peak separation program (Jandel Scientific). Gaussian and/or Lorentzian functions were used to obtain the best fit.

Results and Discussion

Thermodynamic Transitions and Their Corresponding Structural Evolutions. Parts a and b of Figure 1 show two sets of DSC thermograms at different cooling and subsequent heating rates from 2.5 to 20 °C/min, respectively. At the 2.5 °C/min cooling rate (Figure 1a), for example, two partially overlapped exothermic thermal transitions can be observed at 206 and 199 °C. The heats of these two thermal transitions are resolved to be 3.68 and 1.27 kJ/mol, respectively (the inset of Figure 1a). In the lower temperature region, one exothermic transition at 139 °C with a small enthalpy change of 0.37 kJ/mol was found. A glass transition temperature (T_g) appears at 50 °C with a sudden change of heat capacity.

The subsequent heating of 2.5 °C/min (Figure 1b) exhibits the identical thermal transition temperatures with the same heats of transition in the lower temperature region. For the transitions in the higher temperature region, only one apparent endothermic peak with an onset transition temperature of 199 °C and a heat of transition of 4.95 kJ/mol can be observed. In fact, this peak consists of two overlapped endothermic processes (inset of Figure 1b), since the heat of this transition (4.95 kJ/mol) is equal to the summation of those two exothermic heats of transitions at 206 °C (3.68 kJ/mol) and 199 °C (1.27 kJ/mol) observed during cooling. Furthermore, the transition temperatures and the heats of transition of these three transitions are almost independent of cooling and heating rates, as shown in Figure 1a,b.

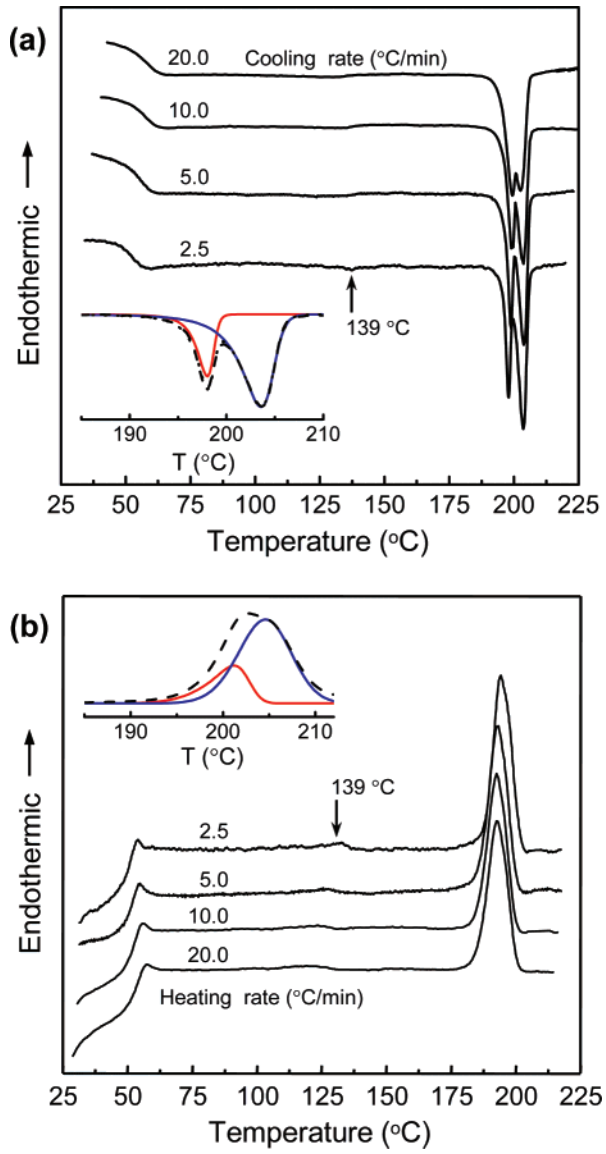

Figure 1. Two sets of DSC (a) cooling and (b) subsequent heating thermal diagrams for the PET(R*-7) polyester at different rates between 2.5 and 20 °C/min. Two insets are the DSC diagrams between 185 and 210 °C, which are resolved utilizing the PeakFit peak separation program. Asymmetric Gaussian and Lorentzian functions were used to obtain the best fit.

Therefore, these three-phase transitions must correspond to the transitions involving LC phases with different types of orders.[32−42]

In order to identify the structural evolutions, 1D WAXD experiments at different temperatures were conducted. A cooling rate of 2.5 °C/min was used in the WAXD experiments to correspond with the DSC results (Figure 1a). Figure 2a shows a set of 1D WAXD powder patterns at different temperatures at a 2.5 °C/min cooling rate. These patterns provide structural information on two length scales. One is on the nanometer scale in the low 2θ angle region between 1.5° and 9°, and the other is on the subnanometer scale between 9° and 40°. Figure 2a shows that above 206 °C this polymer is in the isotropic (I) melt, exhibiting only two broad scattering halos of which their centers are located at $2\theta = 19.3°$ (d-spacing = 0.46 nm) for the high-angle scattering halo and at $2\theta = 3.7°$ (d-spacing = 2.4 nm) for the low-angle scattering halo. They can be assigned as the average lateral distance (0.46 nm) between molecules and the average length (2.4 nm) of the repeat units with liquidlike short-range order.

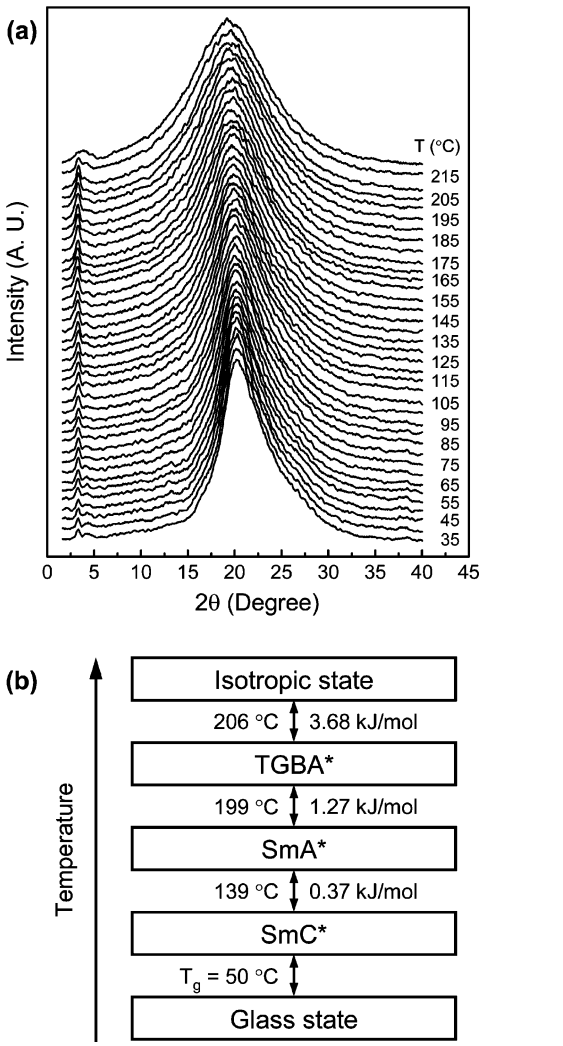

Figure 2. (a) A set of 1D WAXD patterns of the PET(R*-7) polyester at a cooling rate of 2.5 °C/min at different temperatures. (b) Phase transition diagram of the PET(R*-7) polyester with transition temperatures and corresponding enthalpy changes.

At 206 °C, a sharp low-angle diffraction appears at $2\theta = 3.25°$ (d-spacing = 2.72 nm), which usually indicates the formation of a LC phase layer structure, yet there is no higher-order layer diffractions. This transition represents the formation of a TGBA* phase as reported previously for PET(R*-9, -10, and -11).[22,24,28,29] As the temperature decreases to 199 °C, this low-angle diffraction at $2\theta = 3.27°$ (d-spacing = 2.70 nm) increases in intensity and second-order diffractions appear at $2\theta = 6.55°$ (d-spacing = 1.35 nm). In the same temperature range, the center location of the high-angle scattering halo gradually shifts to higher 2θ angles (from 19.3° to 19.7°) and decreases its width. The strong layer diffraction with the higher-order diffractions represents the generation of quasi-long-range order parallel to the layer normal.[32−42] The shifting and narrowing of the high-angle scattering halo during cooling can be attributed to an increase in correlation length and closer molecular lateral packing.[32−42] This diffraction behavior change represents the formation of the SmA* phase (see below for the detailed SmA* phase determination). As the temperature reaches 139 °C, the low-angle diffraction peak shifts suddenly from $2\theta = 3.27°$ to $2\theta = 3.32°$ (d-spacing = 2.65 nm). This represents the thermal transition observed at 139 °C in the DSC thermal diagrams during cooling and heating (Figure 1a,b). This sudden decrease of d-spacing in the low-angle region below 139 °C is attributed to cooperative molecular tilting with respect to layer

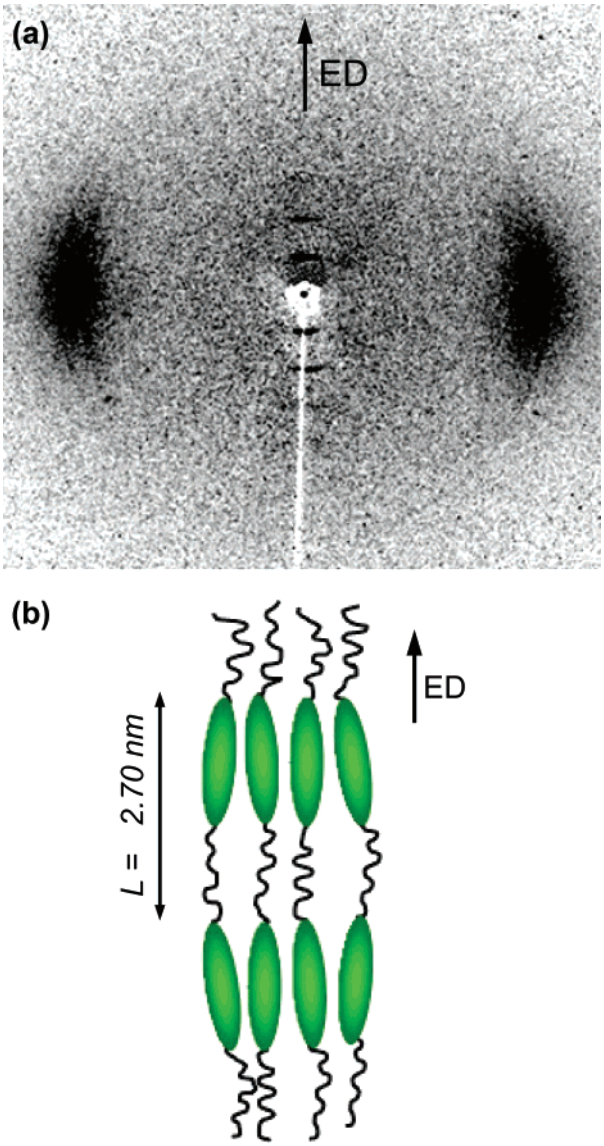

Figure 3. (a) 2D WAXD pattern of the low-ordered SmA* LC phase of PET(R*-7) polyester. The uniaxially elongated film was prepared by the mechanically microextruding and uniaxially drawing at 145 °C and then subsequently quenched to room temperature. The elongated direction (ED) is along the meridian. (b) A schematic chain-packing model for the SmA* LC phase of PET(R*-7) polyester.

normal, representing the transition between the SmA* to the SmC* phase (see below for the detailed SmC* phase determination). After further cooling even below the T_g at 50 °C, no high-angle diffraction peaks can be observed at a cooling rate of 2.5 °C/min, indicating that no crystalline phase developed, which is consistent with the DSC observations (Figure 1a). The 1D WAXD patterns during heating were identical to those during cooling.

The detailed LC structural determinations systematically fit to those reported previously in the cases of PET(R*-9, -10, and -11).[22,24,28,29] We summarize the isobaric structural evolutions of PET(R*-7) with temperature in Figure 2b. Since the SmA* and SmC* phases of PET(R*-7) are critically important precursor phases in this study, we will identify them on the basis of 2D WAXD of oriented samples in the following sections.

Isothermally Crystallized K_M Crystalline Phase in the Oriented SmA* Phase. A 2D WAXD pattern of a uniaxially elongated PET(R*-7) sample at 145 °C is shown in Figure 3a. In this figure, a pair of scattering halos appear, and its center

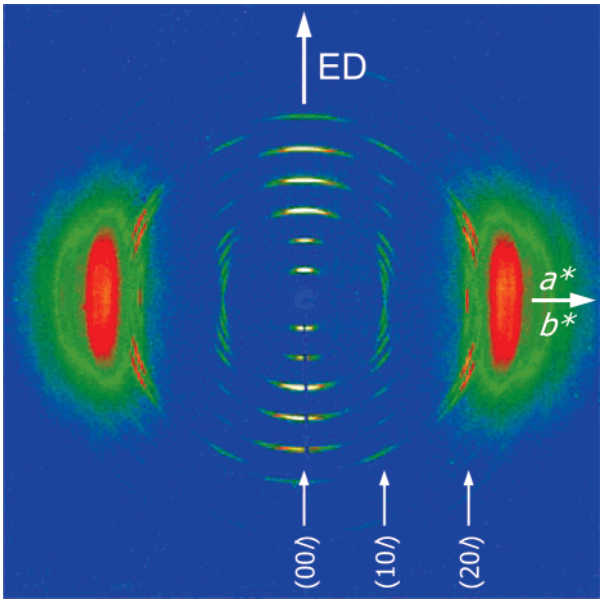

Figure 4. 2D WAXD pattern of the K_M crystalline phase of PET(R*-7) polyester after sample was annealed at 145 °C for 5 days under a nitrogen atmosphere. The elongated direction (ED) and *c**-axis is along the meridian direction while the *a**- and *b**-axes are along the equatorial direction.

location is at $2\theta = 19.7°$ (*d*-spacing = 0.45 nm) with its maximum intensity on the equator. On the meridian, a pair of low-angle diffractions appears at $2\theta = 3.27°$ (*d*-spacing = 2.70 nm) with its high-order diffractions at $2\theta = 6.55°$ (*d*-spacing = 1.35 nm) and $2\theta = 9.82°$ (*d*-spacing = 0.90 nm). These observations indicate that the smectic layer normal is parallel to the elongation direction (ED). The chain molecules are aligned parallel to the ED with liquidlike short-range order in the lateral direction within the layers. Therefore, this low-ordered smectic LC phase can be identified as a chiral smectic A (SmA*) phase,[43] as schematically illustrated in Figure 3b. The measured SmA* layer thickness (2.70 nm) is shorter than the calculated length of the monomer unit (2.92 nm). This difference may be due to the fact that the alkoxyl chains of PET(R*-7) in this SmA* phase contain gauche and trans conformations instead of the all-trans conformation assumed in the Cerius[2] (version 4.6) simulation software based calculation of monomer length.[44−48]

Even though a crystalline phase was not detected during cooling and heating at rates as slow as 2.5 °C/min (Figure 1a,b), PET(R*-7) can be isothermally crystallized by annealing for a prolonged time at a temperature above the T_g under a nitrogen atmosphere. When the oriented PET(R*-7) samples were annealed within the SmA* phase (e.g., at 145 °C) for 5 days, a 2D WAXD pattern exhibits sharp diffractions not only on the equator and meridian but also in the quadrants as shown in Figure 4, indicating the development of a 3D highly ordered crystalline phase. This is a typical fiber pattern with a uniaxial orientation of the crystals along the *c*-axis.

As indicated in Figure 4, the *a**- and *b**-axes are assigned to be on the equator, and the *c** axis is along the ED. On the equator, two strong diffractions appear at $2\theta = 17.14°$ (*d*-spacing = 0.52 nm) and $2\theta = 20.81°$ (*d*-spacing = 0.43 nm) along with a weak diffraction at $2\theta = 22.42°$ (*d*-spacing = 0.397 nm). When the diffractions in the quadrant are projected onto the equator, one extinct diffraction can be identified at $2\theta = 8.55°$ (*d*-spacing = 1.04 nm). This extinct diffraction on the equator at $2\theta = 8.55°$ can be assigned as the (100) diffraction, and it is double the *d*-spacing of the strong diffraction at $2\theta = 17.14°$, which is assigned to be the (200) diffraction. The

Table 1. Experimental and Calculated Crystallographic Parameters of the Monoclinic K_M Crystalline Phase of PET(R*-7) Crystallized at 145 °C

	2θ (deg)		d-spacing (nm)	
hkl	expt[a]	calc[b]	expt[a]	calc[b]
002	3.16	3.16	2.80	2.80
004	6.33	6.33	1.40	1.40
006	9.49	9.48	0.93	0.93
008	12.67	12.69	0.70	0.70
0010	15.86	15.88	0.56	0.56
0012	19.05	19.11	0.47	0.46
101	8.69	8.76	1.02	1.01
102	9.12	9.17	0.97	0.96
103	9.78	9.85	0.90	0.90
104	10.64	10.70	0.83	0.83
106	12.79	12.87	0.69	0.69
107	14.01	14.06	0.63	0.63
108	15.30	15.39	0.58	0.58
200	17.14	17.22	0.52	0.51
204	18.29	18.37	0.49	0.48
205	18.90	19.00	0.47	0.47
208	21.37	21.45	0.42	0.41
$\bar{1}10$	20.81	20.81	0.43	0.43
110	22.42	22.42	0.40	0.40
304	26.62	26.74	0.33	0.33

[a] The accuracy of the experimental data is ±0.005 nm. [b] The calculated data listed are based on the K_M monoclinic unit cell with $a = 1.04$ nm, $b = 0.46$ nm, $c = 5.59$ nm, and $\gamma = 84.2°$.

diffraction at $2\theta = 20.81°$ is attributed to the $(\bar{1}10)$ diffraction, and the weak diffraction at $2\theta = 22.42°$ is the $(\bar{1}10)$ diffraction. On the basis of the unequal *d*-spacings of the (110) and $(\bar{1}10)$ diffractions, we know that the γ angle should not equal 90°. Quantitative calculations indicate that the γ^* angle is 95.8°. We can thus construct the triangle to build a 2D a^*b^* lattice of the unit cell on the basis of the calculated *d*-spacing (0.46 nm) of the (010) diffraction.[49] On the meridian of this pattern, there are six pairs of diffractions at $2\theta = 3.16°$ (*d*-spacing = 2.80 nm), $2\theta = 6.33°$ (*d*-spacing = 1.40 nm), $2\theta = 9.48°$ (*d*-spacing = 0.93 nm), $2\theta = 12.67°$ (*d*-spacing = 0.70 nm), $2\theta = 15.86°$ (*d*-spacing = 0.56 nm), and $2\theta = 19.05°$ (*d*-spacing = 0.47 nm). They should be assigned as the (002) diffraction and its higher orders (004), (006), (008), (0010), and (0012). This assignment is based on the fact that the (*hkl*) diffractions in the quadrants of this 2D WAXD fiber pattern with l = odd numbers are observed in between the neighboring (00*l*) (l = even numbers) diffractions.

Careful structural refinement results in a monoclinic unit cell with dimensions of $a = 1.04$ nm, $b = 0.46$ nm, $c = 5.59$ nm, and $\gamma = 84.2°$, and this phase is labeled as the K_M phase. Table 1 lists the experimentally observed and the calculated 2θ values as well as the *d*-spacings based on this monoclinic unit cell. The calculated crystallographic density is 1.29 g/cm^3, and this agrees with the experimentally observed density (1.27 g/cm^3). Note that the *d*-spacing of the (002) plane (2.80 nm) is larger than the *d*-spacing of the layers in the SmA* phase (2.70 nm).

This structural determination based on the 2D WAXD results is supported by SAED experiments conducted on PET(R*-7) single crystals grown in the SmA* phase (at 145 °C) for 5 days. Both flat-elongated and helical single crystals are observed, as shown in Figure 5a,b. The population of the flat lamellar crystals is below 10%. The helical single crystals of PET(R*-7) are all right-handed. The [00*l*] zone SAED pattern of the flat-elongated single crystal is shown in the inset of Figure 5a. The a^*-axis is defined as the horizontal direction of the SAED pattern, corresponding to the short axis of the lamella in real space. A pair of strong (200) diffractions at a *d*-spacing of 0.52 nm agrees with the 2D WAXD results (Figure 4). By combining both of the strong (*h*l0) and (*h*00) diffractions, a 2D a^*b^* -lattice of the K_M unit cell can be constructed. The measured γ^* angle (95.8°) and *b*-axis unit cell dimension (*d*-spacing = 0.46 nm) agree well the values calculated from the 2D WAXD results (Figure 4).

A SAED pattern obtained from a helical single crystal is inserted into Figure 5b. The diffractions were diffused. The (*hll*) diffraction streaks observed with a *d*-spacing of 0.46 nm correspond to those of the flat single crystals. Diffused (200) diffraction arcs, which correspond to the sharp spots in the flat

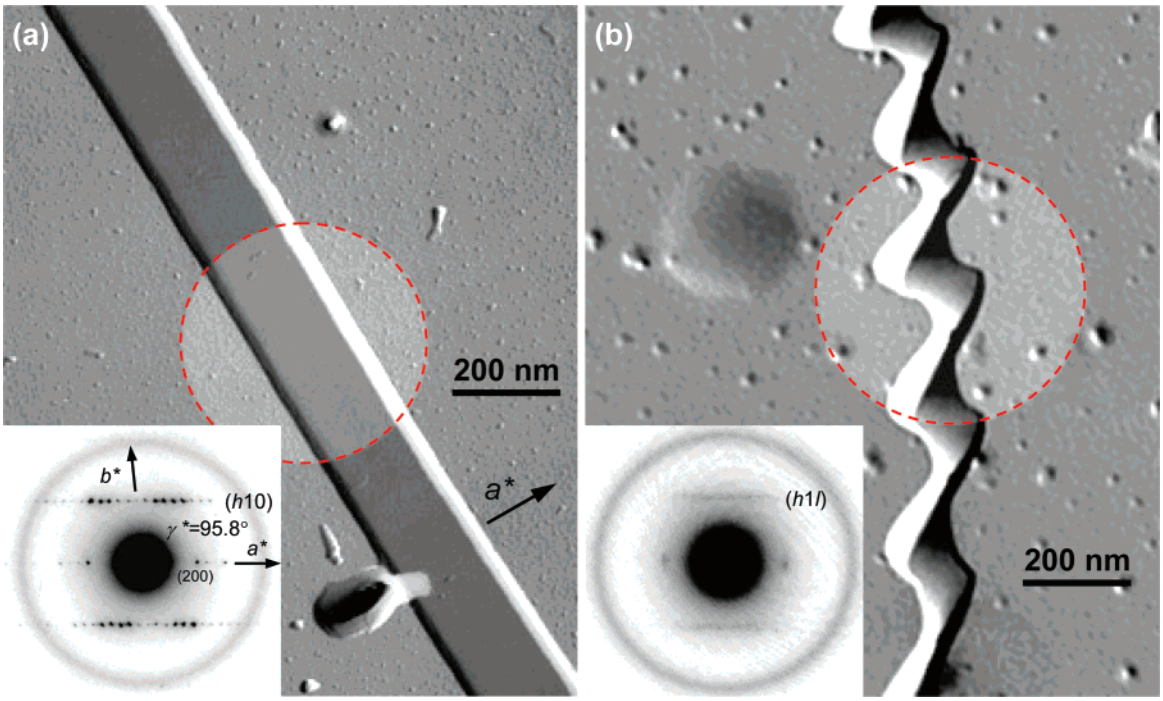

Figure 5. Bright-field TEM morphologies of (a) a flat-elongated lamellar single crystal and (b) a right-handed helical lamellar single crystal of PET(R*-7) polyester. Both lamellar single crystals were crystallized in SmA* phase at 145 °C for 5 days under a nitrogen atmosphere. Two insets are SAED of a flat-elongated lamellar single crystal and a right-handed helical lamellar single crystal of PET(R*-7) polyester, respectively.

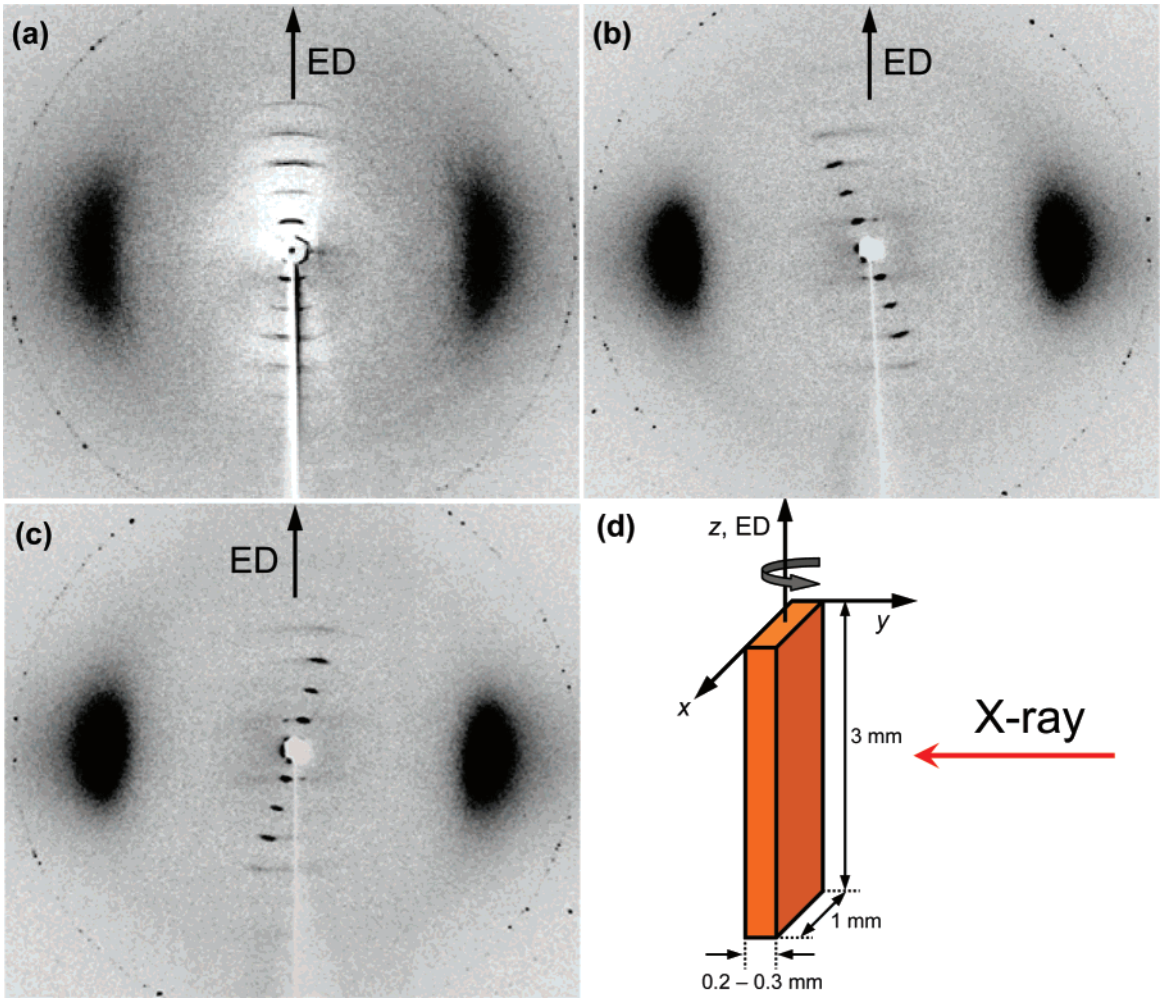

Figure 6. Set of 2D WAXD patterns of a PET(R*-7) monodomain film sample annealed at 135 °C for 16 h in the SmC* phase when the X-ray beam was first aligned normal to (a) the *yz*-plane (along the *x*-axis) and then clockwisely rotated around the *y*-axis for 13°, (b) when the X-ray incident beam was normal to the *xz*-plane of the film (along the *y*-axis), (c) after 180° counterclockwise sample rotation around the *z*-axis, and (d) the monodomain sample geometry illustrated with the right-handed 3D coordinate system.

single crystals, were observed. All of these features indicate the double-twisted helical crystal is identical to those in the cases of PET(R*-*n*) previously reported.[21−29]

Molecular Arrangement of the SmC* Phase in the 3D Monodomain. The 2D WAXD results of the SmC* phase for the uniaxially elongated film samples are shown in Figure 6a−c. The sample was isothermally annealed at 135 °C for 16 h in the SmC* phase and subsequently quenched to below its T_g. The sample geometry is shown with the right-handed 3D coordinate system, as illustrated in Figure 6d. The *x*-axis is along the edge of the ED of the film, the *y*-axis is the film thickness, and the *z*-axis is the ED of the film perpendicular to *xy*-plane. Therefore, the *xz*-plane is parallel to the top surface of the film ("in-plane"), and the *y*-axis is normal to the surface of the film ("out-of-plane"). In order to determine the molecular orientation, 2D WAXD experiments were carried out by aligning the X-ray beam perpendicular to the *yz*-, *xz*-, and *xy*-plane normals with rotating each of the *x*-, *y*-, and *z*-axes. The 2D WAXD patterns shown in Figure 6a−c are the best patterns we could obtain after rotating these axes. In Figure 6a, the incident X-ray beam was first aligned normal to the *yz*-plane (along the *x*-axis), and then, the film was rotated clockwise around the *y*-axis 13°. A pair of scattering halos has a center located at $2\theta = 19.9°$ (*d*-spacing = 0.45 nm) on the equator of Figure 6a represent liquidlike lateral short-range order. In the low-angle region, two

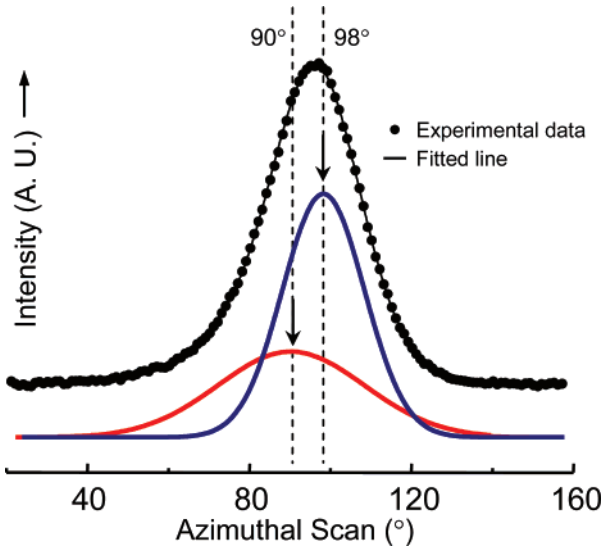

Figure 7. Azimuthal scan of 2θ angle between 18° and 22° in the 2D WAXD pattern of a mechanically oriented SmC* phase of PET(R*-7) polyester when the X-ray beam is perpendicular to the *xz*-plane without sample rotation (Figure 6b). The scattering halos are resolved using the PeakFit peak separation program. Gaussian functions were used to obtain the best fit.

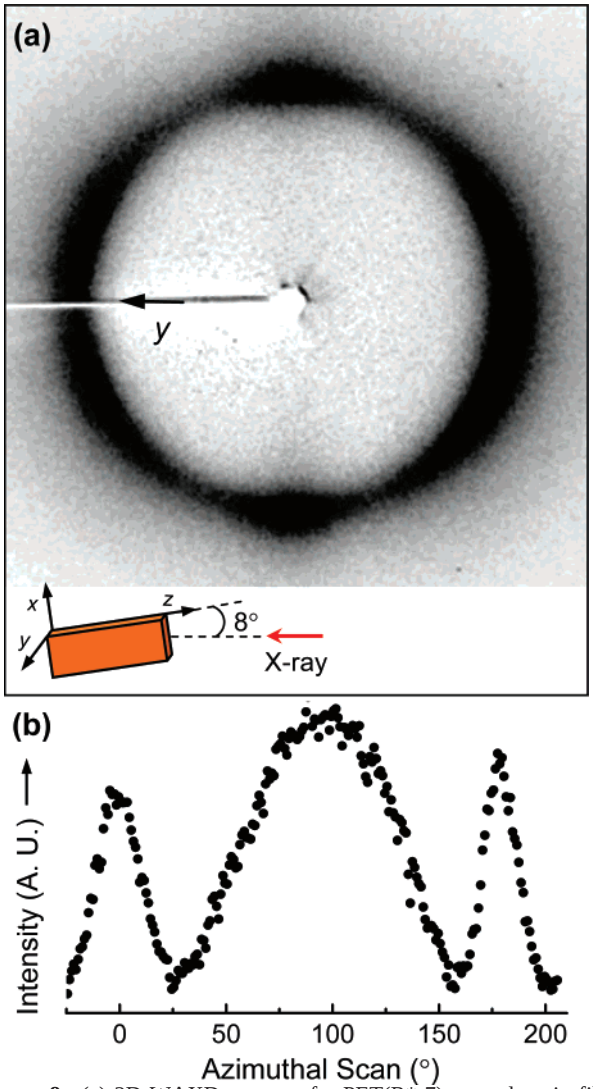

Figure 8. (a) 2D WAXD pattern of a PET(R*-7) monodomain film sample in the SmC* phase which was taken along the direction which is 8° clockwise rotated from the *z*-axis. (b) An azimuthal scan of 2θ angle between 18° and 22° of (a).

sets of strong diffractions appeared at $2\theta = 3.33°$ (*d*-spacing = 2.65 nm) on the meridian (the ED or the *z*-axis) with higher-order diffractions at $2\theta = 6.66°$ (*d*-spacing = 1.33 nm), $2\theta = 10.0°$ (*d*-spacing = 0.88 nm), and $2\theta = 13.35°$ (*d*-spacing = 0.66 nm). Only from the 2D WAXD pattern of Figure 6a, this phase looks like SmA* phase (Figure 3a), but this phase should be SmC* phase on the basis of 1D WAXD patterns (Figure 2a) combined with the DSC results (Figure 1). In order to prove this speculation, 2D WAXD experiments aligned along the *xz*- and *xy*-plane normals of the oriented films were further carried out by rotating each of the *x*-, *y*-, and *z*-axes.

The asymmetric 2D WAXD pattern shown in Figure 6b was obtained by shooting the X-ray normal to the film surface (the *xz* "in-plane") along the *y*-axis. The layer diffraction at $2\theta = 3.33°$ with its higher-order diffractions possess a 13° tilt from the meridian and only appear in the second and fourth quadrants. In the wide-angle region of Figure 6b, subtle but definitive asymmetric scattering halos can be seen, and its center is located at $2\theta = 19.9°$ (*d*-spacing of 0.45 nm) tilted 8° clockwise from the equator opposite from the counterclockwise tilting direction of the layer diffractions in the low-angle region. Therefore, this phase should be assigned as the synclinically tilted SmC* phase. This phase structure identification can be further confirmed by the 2D WAXD pattern (Figure 6c) taken with after rotating the

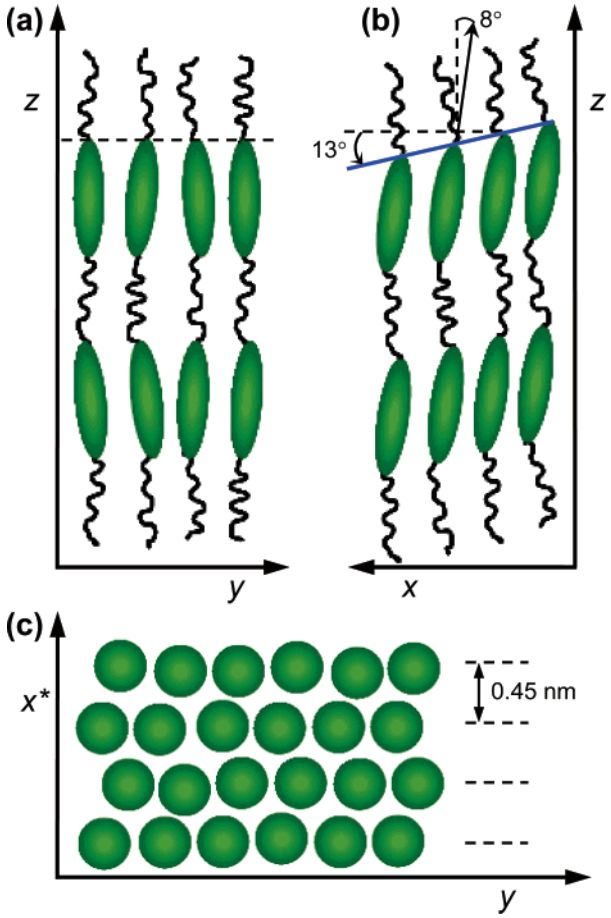

Figure 9. Schematic illustration of the molecular orientation in the SmC* 3D monodomain: (a) on *yz*-plane, (b) on *xz*-plane, and (c) *x***y*-plane.

film 180° around the *z*-axis (Figure 6d). This pattern is a mirror image with respect to the 2D WAXD pattern shown in Figure 6b. Asymmetric scattering halos in the wide angle region can also be observed. It is speculated that the asymmetric scattering halo is comprised of diffuse scattering of more than one halo.

In order to prove this speculation concerning the asymmetric scattering halos, an azimuthal scan of the scattering halos in the 2θ-angle range from 18° to 22° of the pattern in Figure 6b was conducted and is shown in Figure 7. The overlapped scattering halos could be deconvoluted into two halos at azimuthal angles centered at 90° and 98° with a width at half-height of 42.1° and 24.2°, respectively. The question becomes what is the origin of these overlapped scattering halos. These must be associated with the mesogen and flexible spacer orientations within the smectic layers. It is assumed that the flexible spacers of methylene units may be causing the scattering halos along the equator, while the mesogens may be oriented slightly off the equator. However, further studies are necessary to confirm these assignments.

In order to complete the molecular orientation study of the SmC* 3D monodomain, a 2D WAXD pattern was recorded from a film rotated 8° counterclockwise along the *y*-axis from when the incident X-ray beam was along the *z*-axis (perpendicular to the *xy*-plane) (Figure 8a). As expected, no layer diffractions in the low-angle region were observed. To our surprise, however, a pair of scattering spots with symmetric intensity was found on the meridian along with a pair of broad scattering arcs centered on the equator. Both spots and arcs possess the identical *d*-spacing of 0.45 nm (at $2\theta = 19.9°$). The azimuthal scan of the 2θ angle range 18°−22°, in Figure 8a,

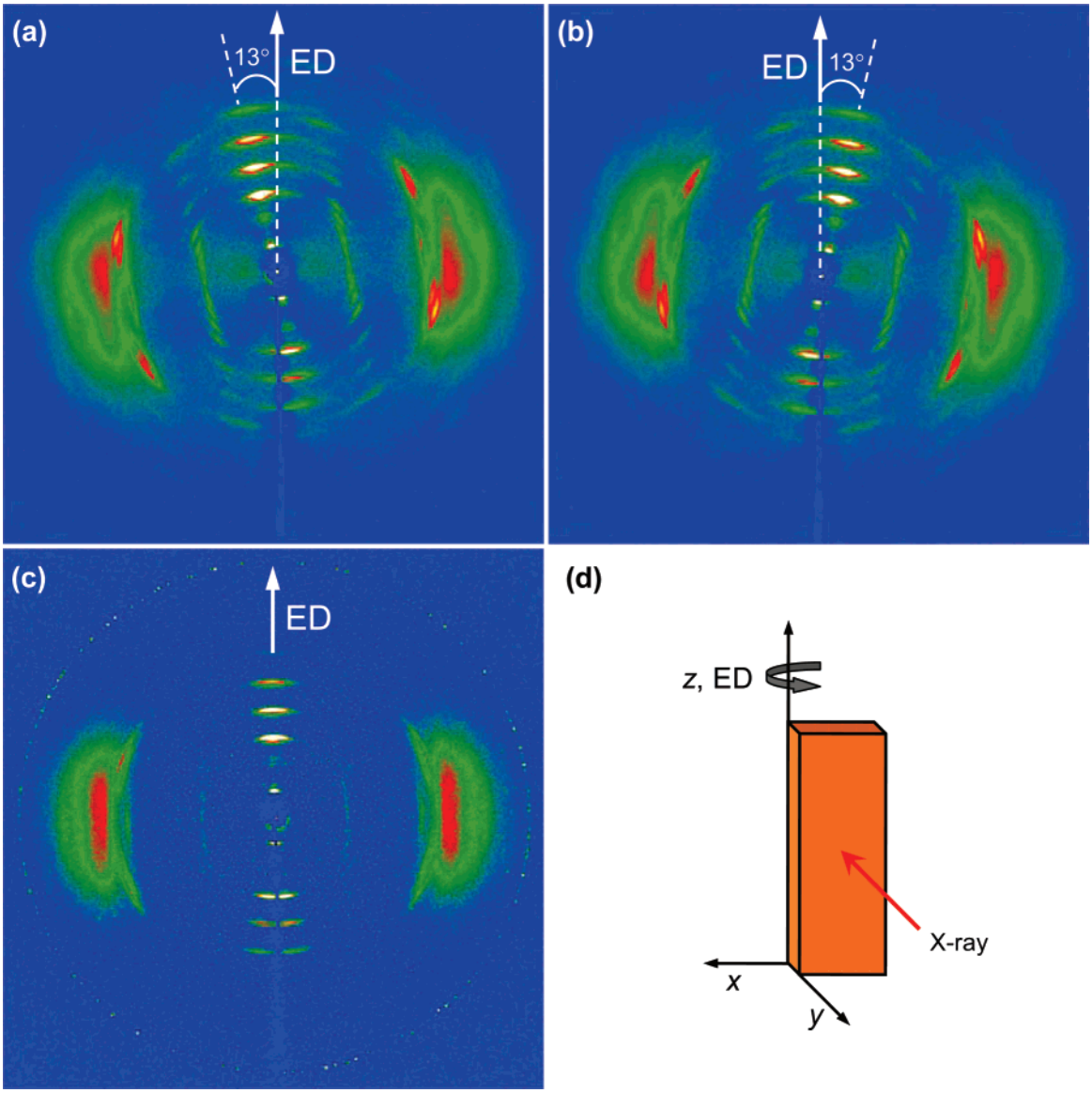

Figure 10. Set of 2D WAXD patterns of K_M crystalline PET(R*-7) polyester. The X-ray beam is perpendicular to the *xz*-plane (a) without the sample rotation around the *y*- or *z*-axis and (b) after 180° counterclockwise sample rotation around the *z*-axis. (c) The X-ray incident beam was first normal to the *xz*-plane, and then a 13° clockwise rotation was applied around *y*-axis. (d) The oriented K_M crystalline sample geometry with the right-handed 3D coordinate system. The K_M crystalline sample is prepared by annealing the 3D monodomain SmC* sample at 135 °C for 5 days under a nitrogen atmosphere.

shows both scattering spots and the arc in Figure 8b. The symmetric pattern generated by the 8° tilting reveals that the mesogen orientation is tilted 8° with respect to the smectic layer normal. The pair of scattering spots reveals that there may be an additional short-range ordered layer structure with its average normal perpendicular to the X-ray beam.

Combining all of the 2D WAXD shown from Figures 6−8, a 3D molecular orientation scheme of the SmC* monodomain can be constructed and is shown in Figure 9. Note that the uniaxial elongation of centimeter-sized films of submillimeter thickness resulted in macroscopic monodomains, and the molecular orientation within the SmC* layers is tilted synclinically ∼21° from the layer normal (Figure 9b). This type of structure may be due to the microextrusion and uniaxial elongation of the sample.

Isothermally Crystallized K_M Crystalline Phase in the SmC* Monodomains. When crystallization is carried out at 135 °C for 5 days in the SmC* phase of the 3D monodomain films, Figure 10a shows the asymmetric 2D WAXD pattern obtained when the X-ray incident direction is along the *y*-axis. The 2D WAXD pattern obtained after rotating the sample 180° along the *z*-axis resembles the mirror image of Figure 10a, as shown in Figure 10b. In both of the figures, the pair of layer diffraction spots with its higher-order diffractions are tilted 13° either counterclockwise (Figure 10a) or clockwise (Figure 10b) from the *z*-axis/ED direction (the meridian). In the high 2θ angle region, all the diffractions are also tilted 13° off of the equator. This indicates that the *c*-axis of the K_M crystal retains the synclinic orientation of the layer normal in the SmC* phase.

Note that in the K_M monoclinic unit cell the γ angle is not 90°. The *c*-axis dimension is 5.59 nm. Each chemical repeat unit in the crystal along the *c*-axis is thus 2.80 nm. This can be compared with the calculated length of the repeating unit which is 2.92 nm. This difference is caused by the helical conformation of the chain molecules in the crystal, which reduces the length of the crystallographic *c*-axis. On the other hand, the layer distance in the SmC* phase is 2.65 nm, indicating chain tilting in the SmC* phase. The molecular orientation/helical axis has to be parallel to the *c*-axis. This implies that at least the mesogens have to drastically reorient from that in the SmC*

phase to that of the K_M phase. As discussed, the mesogen orientation in the SmC* phase is synclinically tilted 21° from the layer normal. If the mesogen is oriented parallel to the *c*-axis, a 21° tilt of the mesogens is necessary for the formation of the crystals in the 3D monodomain. The confinement effect of this SmC* phase on the crystal formation is thus evident.

If we carefully compare the top half and the bottom half of Figure 10a,b, it is evident that both of the 2D WAXD pattern diffraction intensities are not symmetric. This indicates that the *c*-axis of the crystals does not lie in the *xz*-plane. Figure 10c is a 2D WAXD pattern which was taken along the *x*-axis after a clockwise 13° rotation along the *y*-axis. The pattern clearly shows that the top half and bottom half of the diffraction intensities become symmetric, as shown in Figure 10c. The layer diffractions are located on the meridian, indicating that the layer structures of the SmC* phase in the 3D monodomain (Figure 6a) have been retained to become the 13° synclinically tilted single-crystal-like monodomain. Therefore, the K_M phase crystallized from the SmC* phase can be best described as 3D single-crystal-like structures. It is surprising that the relative "soft" smectic LC layer structure can effectively confine the growth of the relatively "hard" crystals by drastically reorienting the molecules into a single-crystal orientation. This is possibly due to the chain lateral packing requirement in the crystal. A final note is that in the 3D monodomain the helical crystals are not observed. This may imply the elongation and external force field are not helpful in forming these helical crystals.

Conclusion

In summary, the phase transitions, structures, and crystallization behaviors of a nonracemic chiral main-chain LC PET-(R*-7) polyester have been investigated. Structural information obtained from WAXD experiments combined with DSC results leads to the identifications of multiple LC phases including TGBA*, SmA*, and SmC* phases, along with a monoclinic (K_M) crystalline phase. Using 2D WAXD experiments of mechanically oriented film and SAED results from single crystals, the K_M crystal structure has been determined to be a unit cell with dimensions: $a = 1.04$ nm, $b = 0.46$ nm, $c = 5.59$ nm, $\alpha = \beta = 90°$, and $\gamma = 84.2°$. Flat-elongated and helical lamellar crystals have been observed by TEM experiments. Helical single crystals are always right-handed. In particular, macroscopic LC 3D monodomain film samples can be obtained by applying uniaxial elongation. The layers in the film samples are synclinically organized in a 13° tilted arrangement with respect to the elongation direction. The molecular orientation in the 3D monodomain films is tilted 8° synclinically with respect to the layer normal. This leads to a 21° tilting with respect to the layer normal. When the isothermal crystallization takes place in the SmC* phase, the chain orientation of the "hard" crystals retains the orientation of the relative "soft" SmC* LC layer normal, indicating a confinement effect of the SmC* phase on the K_M phase. However, when crystallization takes place in the SmA* phase, the *c*-axis (and thus the molecular axis) is along the elongation direction of the samples. This is identical to the layer normal of the SmA* phase, although the *d*-spacing of the (00*l*) planes along the *c*-axis are greater than that of the *d*-spacing in the smectic layers.

Acknowledgment. This work was supported by NSF (DMR-0516602) and the Collaborative Center for Polymer Photonics between the Air Force Research Laboratory Materials and Manufacturing Directorate and The University of Akron. We also acknowledge Perkin-Elmer Co. in providing a Diamond DSC instrument for our laboratory.

References and Notes

(1) Mason, S. F. *Nature (London)* **1984**, *311*, 19.
(2) Barton, J. K. *Science* **1986**, *233*, 727.
(3) Bowden, N. B.; Weck, M.; Choi, I. S.; Whitesides, G. M. *Acc. Chem. Res.* **2001**, *34*, 231.
(4) Lehn, J.-M. *Proc. Natl. Acad. Sci. U.S.A.* **2002**, *99*, 4763.
(5) Declercq, R.; Aerschot, A. V.; Read, R. J.; Herdewijn, P.; Meervelt, L. V. *J. Am. Chem. Soc.* **2002**, *125*, 928.
(6) Whitesides, G. M.; Grzybowski, B. *Science* **2002**, *295*, 2418.
(7) Rozners, E.; Katkevica, D.; Bizdena, E.; Ströemberg, R. *J. Am. Chem. Soc.* **2003**, *125*, 12125.
(8) Tamura, K.; Schimmel, P. *Science* **2004**, *305*, 1253.
(9) Bombelli, C.; Borocci, S.; Lupi, F.; Mancini, G.; Mannina, L.; Segre, A. L.; Viel, S. *J. Am. Chem. Soc.* **2004**, *126*, 13354.
(10) Zubay, G. *Biochemistry*, 2nd ed.; Macmillan Publishing Co.: New York, 1988; pp 845−1151.
(11) Goodby, J. W. *Science* **1986**, *231*, 350.
(12) Helfrich, W.; Prost. J. *Phys. Rev. A* **1988**, *38*, 3065.
(13) Green, M. M.; Peterson, N. C.; Sato, T.; Teramoto, A.; Cook, R.; Lifson, S. *Science* **1995**, *268*, 1860.
(14) Katsaras, J.; Raghunathan, V. A. *Phys. Rev. Lett.* **1995**, *74*, 2022.
(15) Goodby, J. W. In *Handbook of Liquid Crystals*; Demus, D., Goodby, J., Gray, G. W., Spiess, H.-W., Vill, V., Eds.; Wiley-VCH: Weinheim, 1998; Vol. 1, pp 115−132.
(16) Kitzerow, H.-S.; Bahr, C. In *Chriality in Liquid Crystals*; Kitzerow, H.-S., Bahr, C., Eds.; Springer: London, 2001; pp 1−27.
(17) Selinger, R. L. B.; Selinger, J. V.; Malanoski, A. P.; Schnur, J. M. *Phys. Rev. Lett.* **2004**, *93*, 158103-1.
(18) Jeong, K.-U.; Jin, S.; Ge, J. J.; Knapp, B. S.; Graham, M. J.; Ruan, J.; Guo, M.; Xiong, H.; Harris, F. W.; Cheng, S. Z. D. *Chem. Mater.* **2005**, *17*, 2852.
(19) Sung, C. H.; Kung, L. R.; Hsu, C. S.; Lin, T. Z.; Ho, R.-M. *Chem. Mater.* **2006**, *18*, 352.
(20) Jeong, K.-U.; Knapp, B. S.; Ge, J. J.; Jin, S.; Graham, M. J.; Harris, F. W.; Cheng, S. Z. D. *Chem. Mater.* **2006**, *18*, 680.
(21) Li, C. Y.; Yan, D.; Cheng, S. Z. D.; Bai, F.; He, T.; Chien, L. C.; Harris, F. W.; Lotz, B. *Macromolecules* **1999**, *32*, 524.
(22) Li, C. Y.; Yan, D.; Cheng, S. Z. D.; Bai, F.; Ge, J. J.; Calhoun, B. H.; He, T.; Chien, L. C.; Harris, F. W.; Lotz, B. *Phys. Rev. B* **1999**, *60*, 12675.
(23) Li, C. Y.; Cheng, S. Z. D.; Ge, J. J.; Bai, F.; Zhang, J. Z.; Mann, I. K.; Harris, F. W.; Chien, L.-C.; Yan, D.; He, T.; Lotz, B. *Phys. Rev. Lett.* **1999**, *83*, 4558.
(24) Li, C. Y.; Ge, J. J,; Bai, F.; Zhang, J. Z.; Calhoun, B. H.; Chien, L. C.; Harris, F. W.; Lotz, B.; Cheng, S. Z. D. *Polymer* **2000**, *41*, 8953.
(25) Li, C. Y.; Cheng, S. Z. D.; Ge, J. J.; Bai, F.; Zhang, J. Z.; Mann, I. K.; Chien, L. C,; Harris, F. W.; Lotz, B. *J. Am. Chem. Soc.* **2000**, *122*, 72.
(26) Li, C. Y.; Cheng, S. Z. D.; Weng, X.; Ge, J. J,; Bai, F.; Zhang, J. Z.; Calhoun, B. H.; Harris, F. W.; Chien, L. C.; Lotz, B. *J. Am. Chem. Soc.* **2001**, *123*, 2462.
(27) Li, C. Y.; Ge, J. J.; Bai, F.; Calhoun, B. H.; Harris, F. W.; Cheng, S. Z. D.; Chien, L. C.; Lotz, B.; Keith, H. D. *Macromolecules* **2001**, *34*, 3634.
(28) Li, C. Y.; Jin, S.; Weng, X.; Ge, J. J.; Zhang, D.; Bai, F.; Harris, F. W.; Cheng, S. Z. D.; Yan, D.; He, T.; Lotz, B.; Chien, L. C. *Macromolecules* **2002**, *35*, 5475.
(29) Weng, X.; Li, C. Y.; Jin, S.; Zhang, J. J.; Zhang, D.; Harris, F. W.; Cheng, S. Z. D.; Lotz, B. *Macromolecules* **2002**, *35*, 9678.
(30) Lotz, B.; Cheng, S. Z. D. *Polymer* **2005**, *46*, 577 and references cited therein.
(31) Bai, F.; Chien, L. C.; Li, C. Y.; Cheng, S. Z. D.; Percheck, R. *Chem. Mater.* **1999**, *11*, 1666.
(32) Ungar, G.; Feijoo, J. L.; Percec, V.; Yourd, R. *Macromolecules* **1991**, *24*, 953.
(33) Yandrasits, A.; Cheng, S. Z. D.; Zhang, A.; Cheng. J.; Wunderlich, B.; Percec, V. *Macromolecules* **1992**, *25*, 2112.
(34) Pardey, R.; Zhang, A.; Gabori, P. A.; Harris, F. W.; Cheng, S. Z. D.; Adduci, J.; Facinelli, J. V.; Lenz, R. W. *Macromolecules* **1992**, *25*, 5060.
(35) Pardey, R.; Shen, D.; Gabori, P. A.; Harris, F. W.; Cheng, S. Z. D.; Adduci, J.; Facinelli, J. V.; Lenz, R. W. *Macromolecules* **1993**, *26*, 3687.
(36) Yoon, Y.; Zhang, A.; Ho, R.-M.; Cheng, S. Z. D.; Percec, V.; Chu, P. *Macromolecules* **1996**, *29*, 294.
(37) Yoon, Y.; Ho, R.-M.; Moon, B.; Kim, D.; McCreight, K. W.; Li, F.; Harris, F. W.; Cheng, S. Z. D.; Percec, V.; Chu, P. *Macromolecules* **1996**, *29*, 3421.

(38) Zheng, R.-Q.; Chen, E.-Q.; Cheng, S. Z. D.; Xie, F.; Yan, D.; He, T.; Percec, V.; Chu, P.; Ungar, G. *Macromolecules* **1999**, *32*, 3574.
(39) Zheng, R.-Q.; Chen, E.-Q.; Cheng, S. Z. D.; Xie, F.; Yan, D.; He, T.; Percec, V.; Chu, P.; Ungar, G. *Macromolecules* **1999**, *32*, 6981.
(40) Jeong, K.-U.; Knapp, B. S.; Ge, J. J.; Jin, S.; Graham, M. J.; Xiong, H.; Harris, F. W.; Cheng, S. Z. D. *Macromolecules* **2005**, *38*, 8333.
(41) Jeong, K.-U.; Knapp, B. S.; Ge. J. J.; Graham, M. J.; Tu, Y.; Leng, S.; Xiong, H.; Harris, F. W.; Cheng, S. Z. D. *Polymer* **2006**, *47*, 3351.
(42) Shen, H.; Jeong, K.-U.; Xiong, H.; Graham, M. J.; Leng, S.; Zheng, J. X.; Huang, H.; Guo, M.; Harris, F. W.; Cheng, S. Z. D. *Soft Matter* **2006**, *2*, 232.
(43) Seddon, J. M. In *Handbook of Liquid Crystals*; Demus, D., Goodby, J., Gray, G. W., Spiess, H.-W., Vill, V., Eds.; Wiley-VCH: Weinheim, 1998; Vol. 1, pp 635−679.
(44) Bovey, F. A.; Mirau, P. A. *NMR of Polymers*; Academic Press: San Diego, 1996.
(45) Cheng, J.; Jin, Y.; Wunderlich, B.; Cheng, S. Z. D.; Yandrasits, M. A.; Zhang, A.; Percec, V. *Macromolecules* **1992**, *25*, 5991.
(46) Cheng, J.; Yoon, Y.; Ho, R.-M.; Leland, M.; Guo, M.; Cheng, S. Z. D.; Chu, P.; Percec, V. *Macromolecules* **1997**, *30*, 4688.
(47) McElheny, D.; Grinshtein, J.; Frydman, V.; Frydman, L. *Macromolecules* **2002**, *35*, 3544.
(48) Ishida, H.; Horii, F. *Macromolecules* **2002**, *35*, 5550.
(49) Eashoo, M.; Wu, Z.; Zhang, A.; Shen, D.; Tse, C.; Harris, F. W.; Cheng, S. Z. D.; Gardner, K. H.; Hsiao, B. S. *Macromol. Chem. Phys.* **1994**, *195*, 2207.

MA070821P